Biosensors and Bioelectronics 142 (2019) 111483

Contents lists available at ScienceDirect

Biosensors and Bioelectronics

journal homepage: www.elsevier.com/locate/bios

$CuCo_2O_4$/N-Doped CNTs loaded with molecularly imprinted polymer for electrochemical sensor: Preparation, characterization and detection of metronidazole

Yanying Wang[a,1], Lang Yao[a,1], Xin Liu[a], Jing Cheng[a], Wei Liu[a], Tao Liu[b], Mengmeng Sun[a], Lijun Zhao[c], Fang Ding[d], Zhiwei Lu[a], Ping Zou[a], Xianxiang Wang[a], Qingbiao Zhao[e,**], Hanbing Rao[a,*]

[a] College of Science, Sichuan Agricultural University, Xin Kang Road, Yucheng District, Ya'an, 625014, China, PR China
[b] College of Information Engineering, Sichuan Agricultural University, Xinkang Road, Yucheng District, Ya'an, 625014, PR China
[c] Ministry of Agriculture and Rural Affairs Laboratory of Risk Assessment for Quality and Safety of Livestock and Poultry, Chengdu, 610065, PR China
[d] Nanshan District Key Lab for Biopolymers and Safety Evaluation, Shenzhen Key Laboratory of Polymer Science and Technology, Guangdong Research Center for Interfacial Engineering of Functional Materials, College of Materials Science and Engineering, Shenzhen University, Shenzhen, 518060, China, PR China
[e] Key Laboratory of Polar Materials and Devices (MOE), Department of Optoelectronics, East China Normal University, Shanghai, 200241, PR China

ARTICLE INFO

Keywords:
$CuCo_2O_4$
Nitrogen doped carbon nanotubes
Molecularly imprinted polymer
Electrochemical sensor
Metronidazole

ABSTRACT

$CuCo_2O_4$ nanoparticles modified with nitrogen doped carbon nanotubes ($CuCo_2O_4$/N-CNTs) have high specific surface area and good electrical conductivity. Herein, a novel electrochemical sensor based on $CuCo_2O_4$/N-CNTs loaded molecularly imprinted polymer (MIP) modified glassy carbon electrode (GCE) is proposed for rapid and ultrasensitive detection of metronidazole (MNZ). The composite of $CuCo_2O_4$/N-CNTs with MIP significantly enhances the electrical signal. The electrochemical polymerization was performed with MNZ as template and aniline as functional monomer by cyclic voltammetry (CV), and differential pulse voltammetry (DPV) was used to detect MNZ. Factors that affect sensor response were optimized. Under the optimal experimental conditions, the DPV current response shows two linearity ranges for MNZ in the range of 0.005–0.1 μM and 0.1–100 μM with very low limit of detection (LOD) of 0.48 nM (S/N = 3). This electrochemical sensing system has high sensitivity, selectivity, excellent reproducibility, repeatability and stability. The recovery (95.9%–100.9%) and reasonable relative standard deviation (RSD) (3.2%–4.8%) for determination of real samples indicate the practicality of the sensing system. This sensing system has high potential for rapid determination of MNZ in samples such as metronidazole tablets, human serum and urine.

1. Introduction

Metronidazole belongs to the class of 5-nitroimidazole antibiotics, which are mainly used to treat and prevent amebic disease and echinococcosis caused by anaerobic bacteria (Gong et al., 2003). However, since MNZ (Fig. S1) is not biodegradable, toxic effects such as peripheral neuritis, cardiogenic shock, and pseudomembranous colitis occur in clinical applications (Yuan et al., 2015). Methods for detecting MNZ include spectrophotometry (Hatamie et al., 2018), high performance liquid chromatography (HPLC) (Wang et al., 2012) and supercritical fluid chromatography (Bari et al., 1998), etc. Although these methods can accurately and reproducibly detect metronidazole, the pretreatment is often cumbersome, the analysis method can be complicated, and the cost is relatively high (Zhu et al., 2016). Hence, it is imperative to develop a determination method that is highly selective and sensitive to MNZ with low cost (Peng et al., 2012).

Molecular imprinting technology (MIT) which can provide a specific recognition function are widely used (Rao et al., 2018a). Among them, the molecularly imprinted polymers (MIP) prepared by electropolymerization is commonly used because of the simple preparation and controllable film thickness. The functional monomers and template molecules can be electrochemically polymerized (Li et al., 2016). Recognition site is introduced into the polymer membrane by the interaction force between monomer and template (Xiao et al., 2016), then

* Corresponding author.
** Corresponding author.
E-mail addresses: qbzhao@ee.ecnu.edu.cn (Q. Zhao), rhb@sicau.edu.cn (H. Rao).
[1] The authors wish it to be known that, in their opinions, Yanying Wang, Lang Yao should be regarded as joint First Authors.

https://doi.org/10.1016/j.bios.2019.111483
Received 12 June 2019; Received in revised form 24 June 2019; Accepted 26 June 2019
Available online 28 June 2019
0956-5663/

the template molecule is extracted and cavities matching the spatial structure of the template molecule are obtained. Therefore, the template molecule to be determined is specifically recognized by MIP. Electrochemical methods have attracted wide attention due to their high sensitivity, ease of analysis and automation. In electrochemical determination, the target molecules undergo an electrochemical redox process, causing the transfer of electrons, resulting in an increase in current and the onset of redox peak (Liu et al., 2016a). Molecularly imprinted electrochemical sensing systems can combine the advantages of MIP and electrochemical methods.

A variety of nanomaterials were used to modify the electrochemical sensor, such as metal nanoparticles (Beluomini et al., 2017), carbon quantum dot (Pandey and Kant, 2016) and carbon nanotubes (CNTs) (Zhang et al., 2015). Among them, CNTs were widely used due to the high electrical conductivity and large specific surface area (Alizadeh et al., 2019). Doping nitrogen is an effective method to enhance performance (Paraknowitsch and Thomas, 2013; Zhang et al., 2019). On the one hand, nitrogen doping enables the carbon nanotube to have higher conductivity (Maldonado et al., 2006). On the other hand, nitrogen doping enhances the stability of carbon nanotubes (Kim et al., 2011). For example, nitrogen-doped carbon nanotubes (N-CNTs) were used as modification materials for electrodes to enhance the specific surface area and conductivity, and a very low detection limit for Cd and Pb metal ions was obtained (Joshi and Nagaiah, 2015).

Transition metal oxides have excellent electrochemical activity (Jadhav et al., 2016). Among them, $CuCo_2O_4$ nanomaterials have attracted much attention due to low cost, excellent stability and catalytic properties. In addition, $CuCo_2O_4$ nanoparticles have enhanced electrochemical activity, conductivity and specific surface area (Liu et al., 2016c; Pawar et al., 2019; Gao et al., 2019; Xu et al., 2019).

A plethora of electrochemical sensing systems for the detection of MNZ have been developed. For example, Ensafi et al. (Ensafi et al., 2018a) reported a sensing system of graphene nanosheet loaded with graphene quantum dot modified by molecularly imprinted polymer for electrochemical detection of metronidazole. Li et al. (Li et al., 2015) reported an electrochemical sensing system of molecularly imprinted polymer modified nanoporous nickel framework for the detection of metronidazole. Chen et al. (Chen et al., 2013) developed a core-shell molecularly imprinted polymer modified sensing system for electrochemical detection of metronidazole. In these reports, the specific surface area was increased by modifying the nanomaterial on the electrode, and a larger quantity of MIP was loaded and more MIP cavities were created, thereby more MNZ can be adsorbed. However, the performance of an electrochemical sensor depends not only on the number of recognition sites but also on the conductivity of the modifying material (Gomes et al., 2019). The enhanced conductivity improves electron transfer and a lower detection limit can be obtained. Therefore, the preparation of MIP on nanomaterials with high electrical conductivity is critical to the development of sensors. Moreover, it is important to prepare a sensor that can analyze MNZ in a variety of samples.

In this study, we developed an electrochemical sensor based on $CuCo_2O_4$/N-CNTs/MIP for ultra-sensitive and selective determination of MNZ. $CuCo_2O_4$/N-CNTs were used to increase the sensitivity of the sensor by increasing the electrochemically active area and electronic transfer capability. MIP was used to increase the selectivity of the sensor. The experimental process is illustrated in Scheme 1, multi-walled carbon nanotubes were oxidized and $CuCo_2O_4$/N-CNTs were synthesized by one step hydrothermal method. $CuCo_2O_4$/N-CNTs were loaded on the surface of the electrode to enhance electrochemical signals. Subsequently, the template molecule MNZ with the electrochemically active functional monomer aniline were electropolymerized on the $CuCo_2O_4$/N-CNTs modified electrode, and specific recognition sites for MNZ were formed. After extracting the template molecule, cavities matching the MNZ spatial structure and binding site is obtained, and MNZ is re-adsorbed by π-π stacking and hydrogen bonding interaction. The performance for the electrochemical determination of MNZ was evaluated by CV, DPV and electrochemical impedance spectroscopy (EIS). The composite of $CuCo_2O_4$/N-CNTs and MIP enables electrochemical sensing system to rapidly, selectively and sensitively determine MNZ in a variety of actual samples, including metronidazole tablets, human serum and urine.

2. Experimental

2.1. Reagents and apparatus

Supporting material details the experimental reagents and apparatus.

2.2. Oxidization of multi-walled carbon nanotubes

The oxidation step of multi-walled carbon nanotubes (MWCNTs) is as follows: firstly, 23 mL of concentrated sulfuric acid and 100 mg of MWCNT were added to the flask and stirred for 12 h. Then, 416 mg of KNO_3 was added, followed by slowly addition of 1 g of $KMnO_4$ in water bath at 40 °C, and stirring for 30 min. Then 3 mL of ultrapure water was added. After 5 min, 3 mL of ultrapure water was added. After another 5 min, 40 mL ultrapure water was added. 15 min later, 10 mL H_2O_2 (30%) and 140 mL ultrapure water were added to terminate the MWCNT oxidation reaction. The oxidized MWCNTs were collected by centrifugation, washed with ultrapure water and 5% HCl solution to neutrality, and finally freeze-dried.

2.3. Preparation of $CuCo_2O_4$/N-CNTs/GCE

Briefly, 0.068 g of oxidized MWCNTs were dispersed in 4 mL of ultrapure water and 96 mL of ethanol with ultrasonication. Subsequently, 0.128 g of $Cu(OAc)_2{\cdot}H_2O$ and 0.319 g of $Co(OAc)_2{\cdot}4H_2O$ were added to the MWCNT-EtOH suspension, followed by the addition of 0.5 mL of $NH_3{\cdot}H_2O$ at room temperature. The reaction was carried out with stirring at 80 °C for 20 h. Then, the reaction mixture was transferred to a 100 mL autoclave, and hydrothermal reaction was carried out at 150 °C for 1 h. The target product was centrifuged and collected, washed repeatedly with ultrapure water and ethanol, and finally freeze-dried. 2 mg of $CuCo_2O_4$/N-CNTs were ultrasonically dispersed in 1 mL of ultrapure water, and then 10 μL of the suspension (2 mg mL^{-1}) was added dropwise to the surface of the GCE and dried at room temperature. The electrode pretreatment procedures are as follows: 0.02–0.05 μm alumina aqueous slurry was evenly applied onto the suede, on which the GCE surface was then polished. The GCE was ultrasonically cleaned with 1:1 HNO_3 (v/v) and ethanol for 5 min, washed with ultrapure water and dried at room temperature.

2.4. Preparation of $CuCo_2O_4$/N-CNTs/MIP/GCE

Firstly, 0.1 M phosphate buffer solution (PBS) solution containing 44 mM aniline and 11 mM MNZ was ultrasonicated for 5 min and placed in the dark for 30 min. The MIP film was prepared on the surface of $CuCo_2O_4$/N-CNTs/GCE by CV electropolymerization for 2 cycles. The potential range was −0.2–1.2 V, the initial scan polarity was positive, the scan rate was 50 mV s^{-1}, the sample interval was 0.001 V, the quiet time was 2 s, and the sensitivity was 1.00×10^{-3} A V^{-1}. After the completion of the electropolymerization, the electrode was immersed in a methanol-acetic acid (v:v = 9:1) solution and gently stirred with a magnetic stirrer for 6 min to extract the template molecules from the polyaniline film. In order to further remove the template molecules, the electrodes were immersed in 0.1 M PBS solution for electrochemical elution by cyclic voltammetry in the potential range of −1.0 to 0 V. The initial scan polarity was positive, the scan rate was 50 mV s^{-1}, the number of cycles was 5, the sample interval was 0.001 V, the quiet time was 2 s, and the sensitivity was 1.00×10^{-4} A V^{-1}. NIP modified

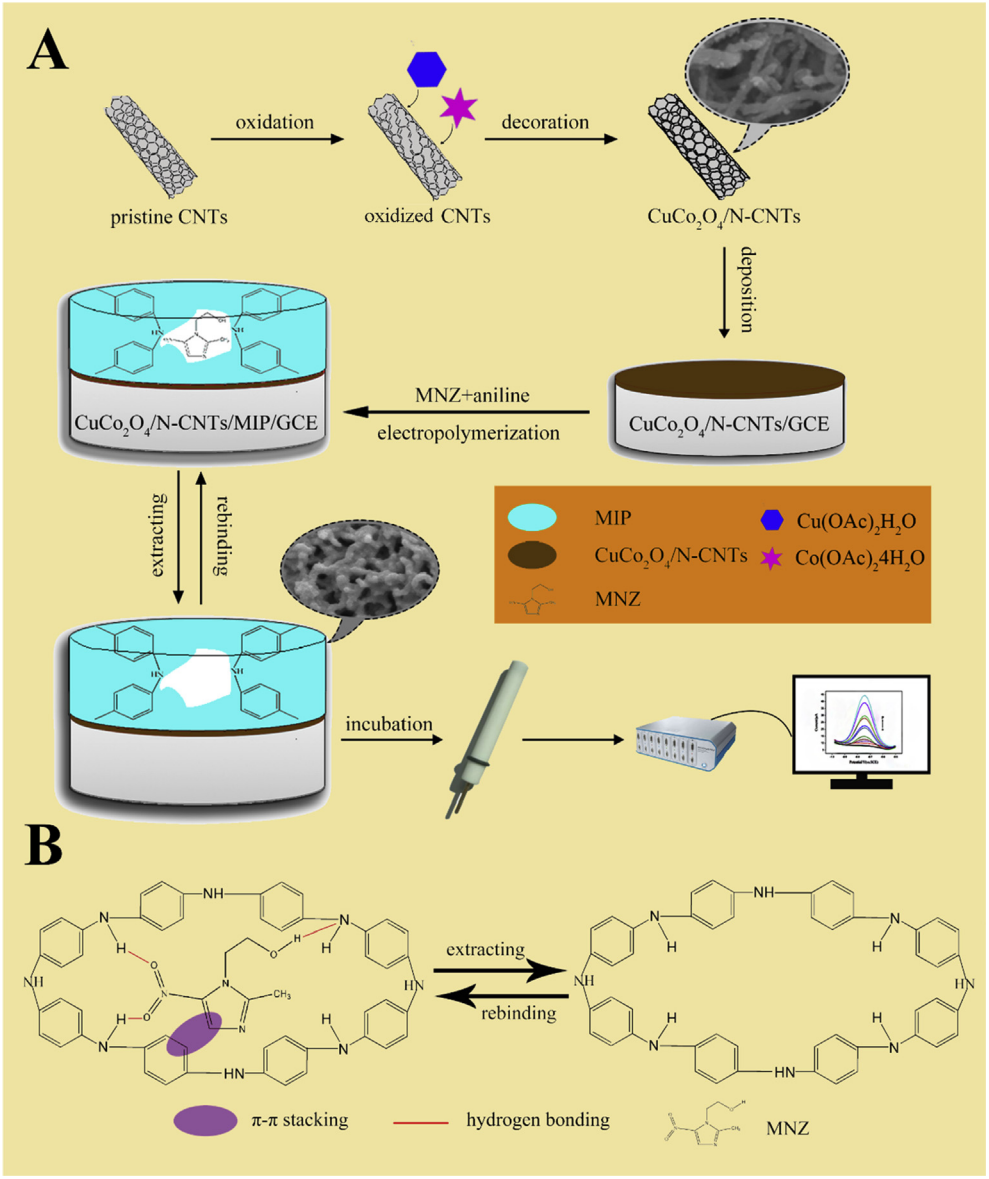

Scheme 1. Schematic diagram for preparation of $CuCo_2O_4$/N-CNTs/MIP/GCE and electrochemical determination of metronidazole (A), elution and resorption of template molecules (B).

electrodes were prepared by the same method without MNZ template.

3. Results and discussion

3.1. Characterization of $CuCo_2O_4$/N-CNTs, $CuCo_2O_4$/N-CNTs/MIP, $CuCo_2O_4$/N-CNTs/NIP

Scanning electron microscopy (SEM), transmission electron microscopy (TEM), power X-ray diffraction (XRD), energy-dispersive spectrometry (EDS), X-ray photoelectron spectroscopy (XPS) were used to characterize the morphology, crystal structure, elemental composition and valence state of the modified electrode surfaces. As shown in Fig. 1A, the $CuCo_2O_4$/N-CNTs nanomaterial has a tubular structure. Fig. 1A indicates that the $CuCo_2O_4$ nanoparticles have been modified on the N-CNTs, and Fig. 1B shows the distribution of nanoparticles on the surface of the N-CNTs. Fig. 1C and D shows the SEM images of $CuCo_2O_4$/N-CNTs/MIP and $CuCo_2O_4$/N-CNTs/NIP, respectively. The $CuCo_2O_4$/N-CNTs/NIP has an irregular spherical structure. In contrast, the $CuCo_2O_4$/N-CNTs/MIP has a rough and porous structure, which was likely caused by the elution step.

The phase composition of $CuCo_2O_4$/N-CNTs nanocomposites was characterized by XRD, as shown in Fig. S2A. The diffraction peaks were assigned to the spinel $CuCo_2O_4$ phase (PDF#37–0878), indicating successful synthesis of $CuCo_2O_4$. In addition, $CuCo_2O_4$/N-CNTs/MIP (before and after elution) and $CuCo_2O_4$/N-CNTs/NIP were characterized by XRD. After electropolymerization of MIP on the surface of $CuCo_2O_4$/N-CNTs, the peak shape of the XRD pattern obtained for $CuCo_2O_4$/N-CNTs/MIP changed significantly (Fig. S2B, a). There is no characteristic peak of $CuCo_2O_4$/N-CNTs, indicating that $CuCo_2O_4$/N-CNTs are completely encapsulated by MIP. After the template molecules were extracted by the elution step, the XRD patterns of $CuCo_2O_4$/N-CNTs/MIP changed slightly (Fig. S2B, b). This is likely due to the formation of a molecularly imprinted cavities. Compared with $CuCo_2O_4$/N-CNTs, the XRD patterns of $CuCo_2O_4$/N-CNTs/NIP changed significantly (Fig. S2B, c). Similarly, the characteristic peaks of $CuCo_2O_4$/N-CNTs did not appear, indicating that $CuCo_2O_4$/N-CNTs were completely encapsulated by NIP. The elemental distribution of $CuCo_2O_4$/N-CNTs was characterized by element mapping. EDS spectrums of $CuCo_2O_4$/N-CNTs are shown in Fig. S2D. Co, Cu and O elements are uniformly distributed on the surface of N-CNTs (Fig. S2C), indicating that the $CuCo_2O_4$

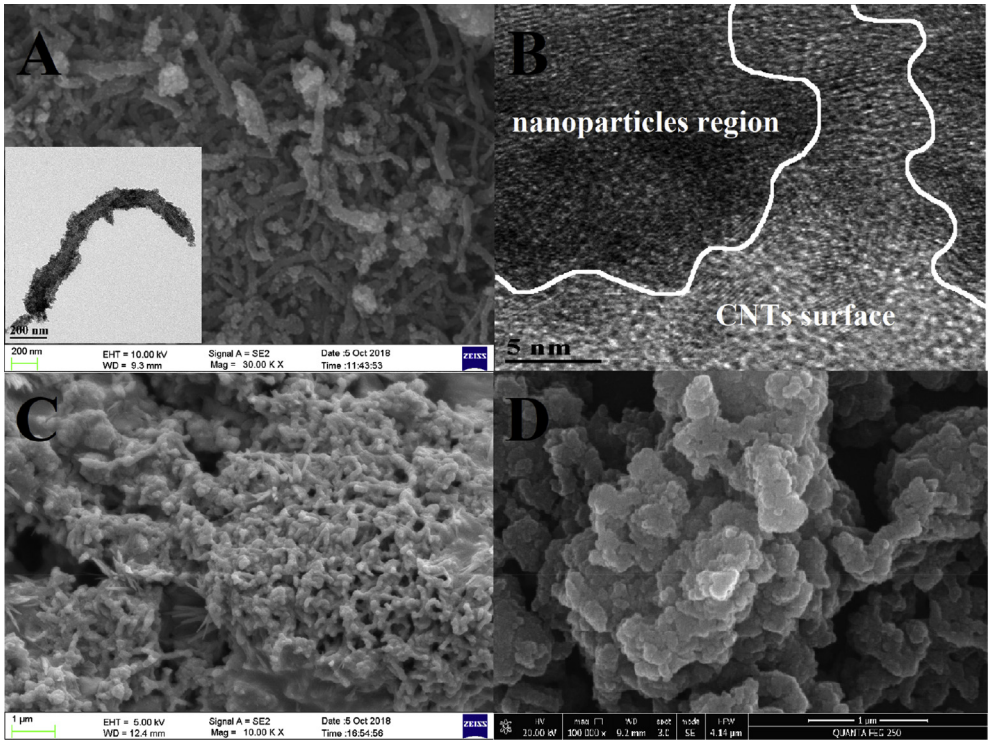

Fig. 1. (**A**) SEM image of $CuCo_2O_4$/N-CNTs. The inset is the TEM image of $CuCo_2O_4$/N-CNTs. (**B**) TEM image of $CuCo_2O_4$/N-CNTs (**C**) $CuCo_2O_4$/N-CNTs/MIP (**D**) $CuCo_2O_4$/N-CNTs/NIP.

nanoparticles are uniformly distributed in the N-CNTs.

The XPS analysis of $CuCo_2O_4$/N-CNTs nanocomposites was performed. The full spectrum is shown in Fig. S3A. In the Cu 2p spectrum (Fig. S3B), the peaks at 934.4 and 954.5 eV are attributed to Cu $2p_{3/2}$ and Cu $2p_{1/2}$, respectively. In addition, two satellite peaks at 941.7 and 962.1 eV are characteristic of Cu^{2+} (Guo et al., 2015). As shown in the Co 2p spectrum (Fig. S3C), the Co $2p_{3/2}$ and Co $2p_{1/2}$ peaks are located at 780.1 and 795.0 eV, respectively. By deconvolution, it is shown that $CuCo_2O_4$/N-CNTs contain two cobalt ions, including Co^{3+} at 779.8 eV and Co^{2+} at 781.4 eV (Fig. S3D). By deconvolution of the O 1s spectrum (Fig. S3E), the peak at 529.8 eV is derived from the metal-oxygen bond, the peak at 531.4 eV is from oxygen vacancy (Liu et al., 2016b) and the peak at 532.8 eV is attributed to the carbon-oxygen bond (Tong et al., 2015). The chemical environment of $CuCo_2O_4$ nanoparticles was studied by analyzing C 1s and N 1s spectra. In the C 1s spectrum (Fig. S3F), by deconvolution, the C=O bond and the C–C bond are at 288.2 eV and 284.6 eV, respectively. The C–N bond at 285.7 eV indicates that N has been doped into the CNTs. By deconvolution of the N 1s spectrum (Fig. S3G), the nanocomposite contains pyridinic N and metal-N at 398.3 eV and 399.8 eV, respectively.

In order to evaluate the porosity and specific surface area of $CuCo_2O_4$/N-CNTs, characterization was performed using Brunner-Emmet-Teller (BET). As shown in Fig. S4A, the N_2 adsorption-desorption isotherm of $CuCo_2O_4$/N-CNTs shows a clear isothermal hysteresis, belonging to the type IV of the International Union of Pure and Applied Chemistry (IUPAC) classification system. This proves the mesoporous structure of $CuCo_2O_4$/N-CNTs. As shown in Fig. S4B, the pore size distribution of $CuCo_2O_4$/N-CNTs indicates that it has no micropores (< 2 nm). $CuCo_2O_4$/N-CNTs mainly contain mesopores (2 nm–50 nm) and a small number of macropores (> 50 nm). The pore volume and specific surface area of $CuCo_2O_4$/N-CNTs were 0.51 cm^3/g and 72.80 m^2/g, respectively, indicating that $CuCo_2O_4$/N-CNTs have a large porosity and specific surface area.

3.2. Electrochemical characterization of the modified electrodes

In order to characterize the electrical conductivity of different electrodes, cyclic voltammetry was used for the electrochemical characterization of the bare electrode and the modified electrode in 5.0 mM $[Fe(CN)_6]^{3-/4-}$ and 0.5 M KCl (Zhang et al., 2010). The potential range was from −0.2 V to 0.6 V and the scan rate was 50 mV s^{-1}. As shown in Fig. 2A, curve a shows a pair of pronounced potassium ferrocyanide redox peaks for bare GCE with peak potentials of 0.22 V and 0.31 V, respectively. As GCE was modified by N-CNTs, the peak current of N-CNTs/GCE was significantly enhanced (curve b), indicating that N-CNTs have good electrical conductivity. As GCE was modified by $CuCo_2O_4$, the peak current of $CuCo_2O_4$/GCE was also enhanced (curve c), indicating that $CuCo_2O_4$ has good electrical conductivity. Furthermore, as GCE was modified by $CuCo_2O_4$/N-CNTs, the peak current of $CuCo_2O_4$/N-CNTs/GCE is further enhanced (curve d). This indicates that the nanocomposite $CuCo_2O_4$/N-CNTs has strong electron transfer ability, which plays an important role in improving sensitivity. After electropolymerization of MIP, a dense polyaniline film forming on the surface of the electrode hinders the electron conduction. Thus, the current response was significantly reduced (curve e), showing a smooth curve. After extracting the template molecules by the elution solution, MNZ imprinted cavities were formed on MIP film, which increased the electron transfer rate. The peak current of $CuCo_2O_4$/N-CNTs/MIP/GCE after elution (curve f) is significantly larger than the that of $CuCo_2O_4$/N-CNTs/MIP/GCE before elution (curve e). Since conductivity of polyaniline is lower than that of $CuCo_2O_4$/N-CNTs, the current response of $CuCo_2O_4$/N-CNTs/MIP/GCE after elution (curve f) is lower than $CuCo_2O_4$/N-CNTs/GCE (curve d). In comparison, after electropolymerizing non-imprinted polymer (NIP) and performing an elution step, the current response was significantly reduced (curve g). $CuCo_2O_4$/N-CNTs/MIP/GCE with template molecules removed has a strong current response due to the presence of molecularly imprinted cavities and surface enhancement effects.

EIS can be used to characterize the resistance of different electrodes.

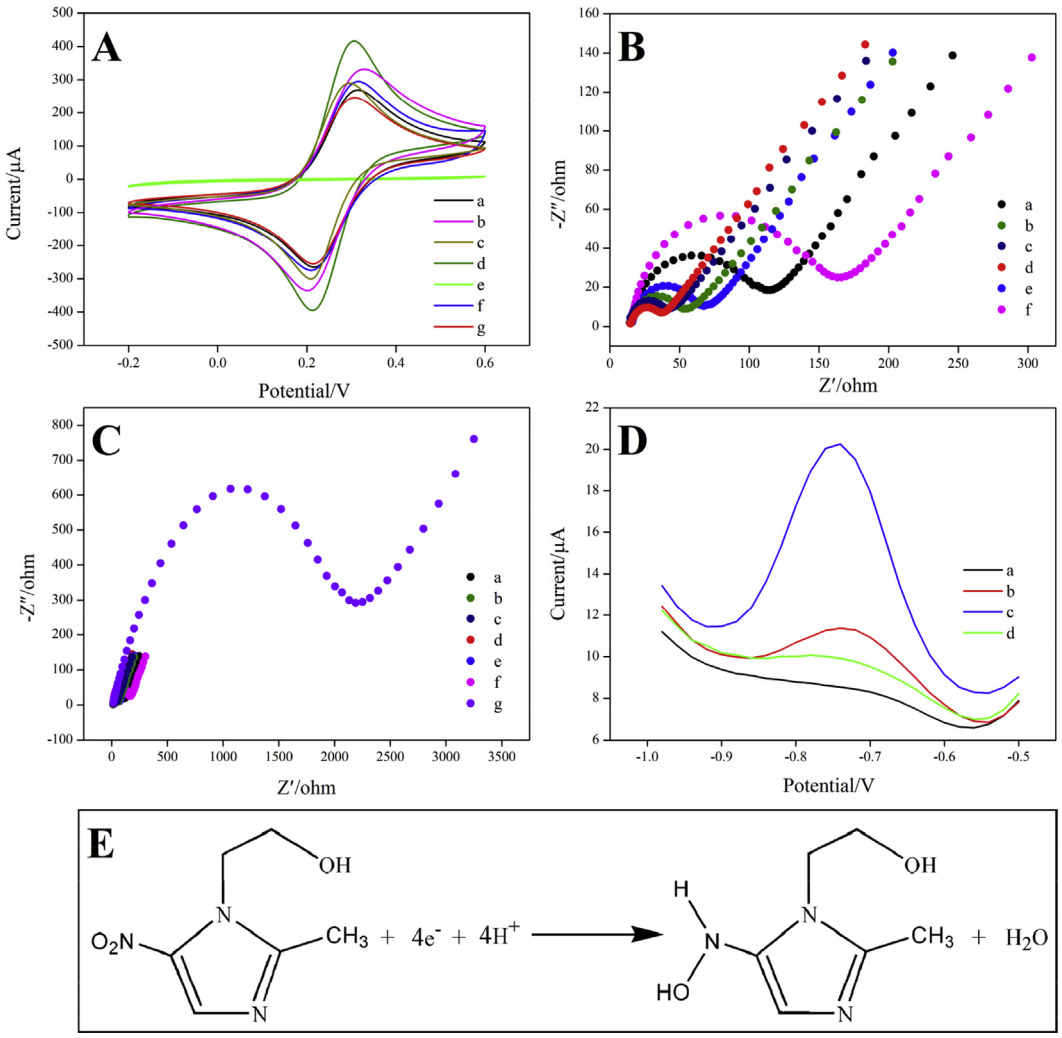

Fig. 2. (**A**) CV characterization of different electrodes in 5.0 mM $[Fe(CN)_6]^{3-/4-}$ and 0.5 M KCl, bare GCE (a), N-CNTs/GCE (b), $CuCo_2O_4$/ GCE (c), $CuCo_2O_4$/N-CNTs/GCE (d), $CuCo_2O_4$/N-CNTs/MIP/GCE before elution (e), $CuCo_2O_4$/N-CNTs/MIP/GCE after elution (f), $CuCo_2O_4$/N-CNTs/NIP/GCE (g); (**B**) EIS of bare GCE (a), $CuCo_2O_4$/GCE (b), N-CNTs/GCE (c), $CuCo_2O_4$/N-CNTs/GCE (d), $CuCo_2O_4$/N-CNTs/MIP/GCE after elution (e), and $CuCo_2O_4$/N-CNTs/NIP/GCE (f) in 5.0 mM $[Fe(CN)_6]^{3-/4-}$ and 0.5 M KCl; (**C**) EIS of $CuCo_2O_4$/N-CNTs/MIP/GCE before elution (g), where a, b, c, d, e and f are the same as in (**B**); (**D**) DPV characterization of bare GCE (a), $CuCo_2O_4$/N-CNTs/GCE (b), $CuCo_2O_4$/N-CNTs/MIP/GCE (c), $CuCo_2O_4$/N-CNTs/NIP/GCE (d) in PBS (0.1 M, pH = 10.0) incubating 20 μM MNZ; (**E**) Schematic diagram of the reduction mechanism of MNZ.

The semicircular and linear portions of the Nyquist impedance spectrum represent the charge transfer resistance (R_{ct}) and diffusion process, respectively. In this study, EIS was used to characterize bare electrodes and different modified electrodes in a 5.0 mM $[Fe(CN)_6]^{3-/4-}$ solution. As shown in Fig. 2B, the R_{ct} of $CuCo_2O_4$/GCE (b) and N-CNTs/GCE (c) are lower than that of the bare electrode (a). This is because $CuCo_2O_4$ and N-CNTs with good conductivities facilitate the electron transfer. Furthermore, the R_{ct} of $CuCo_2O_4$/N-CNTs/GCE (d) is lower than that of $CuCo_2O_4$/GCE (b) and N-CNTs/GCE (c). This is because $CuCo_2O_4$/N-CNTs has a large ratio of surface area to volume and good conductivity, which promote the electron transfer rate. Compared with $CuCo_2O_4$/N-CNTs/GCE, the R_{ct} of the eluted $CuCo_2O_4$/N-CNTs/MIP/GCE (e) increased, which was attributed to the low conductivity of polyaniline film. Since the target molecules can undergo redox reaction through the molecularly imprinted cavities on the MIP, the R_{ct} of $CuCo_2O_4$/N-CNTs/MIP/GCE is much lower than that of $CuCo_2O_4$/N-CNTs/NIP/GCE (f), further indicating the formation of molecularly imprinted cavities. As shown in Fig. 2C, the R_{ct} of $CuCo_2O_4$/N-CNTs/MIP/GCE before elution (g) is the largest, probably because the template molecule occupies the molecularly imprinted cavity and it is difficult for potassium ferricyanide to undergo redox reaction.

To evaluate the resorption capacity of $CuCo_2O_4$/N-CNTs/MIP/GCE, a 20 μM MNZ solution in 0.1 M PBS was prepared and tested using DPV (Fig. 2D). The modified electrodes were pre-adsorbed by MNZ with gentle agitation under a magnetic stirrer for 60 s, followed by DPV in the potential range of −1.0 to −0.5 V, with the amplitude of 0.12 V, pulse width of 0.15 s, pulse period of 0.5 s, and quiet time of 2 s.

According to previous studies, MNZ is an electrochemically active substance whose electrochemical reduction process follows a four-electron/four-proton mechanism (Gu et al., 2016b). Therefore, $CuCo_2O_4$/N-CNTs/MIP/GCE follows two steps for the sensing mechanism of MNZ: Firstly, the molecularly imprinted cavities formed in the MIP specifically bind to MNZ. Subsequently, $CuCo_2O_4$/N-CNTs/MIP realizes the electrochemical reduction of MNZ. Since the process involves the transfer of four electrons, as the sensor detects MNZ using an electrochemical method, a current response is generated. A higher concentration of MNZ leads to more electron transfer numbers generated by $CuCo_2O_4$/N-CNTs/MIP/GCE in the electrochemical reduction process of MNZ. Thus, the peak current of MNZ is increased, and the MNZ reduction peak appearing on the corresponding electrochemical spectrum is stronger, and electrochemical determination can be performed. Due to the electrochemical reduction process (Fig. 2E), MNZ

has a strong reduction peak at −0.74 V. The peak current of the bare electrode is very low (curve a). With $CuCo_2O_4$/N-CNTs modified GCE, the current response was significantly enhanced (curve b). After electropolymerization of MIP on $CuCo_2O_4$/N-CNTs/GCE surface and elution, the current response (curve c) was 5.2 times stronger than that of non-imprinted electrode (curve d), indicating that the MNZ imprinted MIP can specifically recognize MNZ, and has good resorption capacity.

3.3. Electrochemical parameter calculation

According to the Randles-Sevcik equation, the electroactive surface area of the sensing system is 0.263 cm^2. The electron transfer coefficient was calculated to be 0.680. In addition, the surface concentration and diffusion coefficient calculated from the Cottrell equation are 1.08×10^{-11} mol cm^{-2} and 2.137×10^{-4} cm^{-2} s^{-1}, respectively. The standard rate constant calculated from the Velasco equation is 0.12×10^{-1} cm s^{-1}. Detailed calculation of each parameter is included in the Supporting material.

3.4. Conditional optimization

Supporting material details the optimization of the concentration of $CuCo_2O_4$/N-CNTs, the molar ratio of template molecule to functional monomer, the number of electropolymerization cycles, pH, incubation and elution time.

3.5. Performance evaluation

3.5.1. Calibration curve and detection limit

Due to the low background current and high sensitivity of DPV, the reduction peak can be observed for very low concentration of MNZ. Under the optimal determination conditions, the electrochemical response of $CuCo_2O_4$/N-CNTs/MIP/GCE to MNZ in various concentrations was evaluated. As shown in Fig. 3A, it can be seen that the peak current increases with higher MNZ concentration. Two independent linear relationships are exhibited in the concentration range of 0.005–0.1 μM and 0.1–100 μM. The linear regression equations are I_p (μA) = 0.5328 + 4.1901c (μM), R^2 = 0.9991 (Fig. 3C) and I_p (μA) = 1.0942 + 0.3462c (μM), R^2 = 0.9946 (Fig. 3D, black curve). In addition, LOD was calculated according to the following equation: LOD = 3 σ/*S* (n = 10) (Atar et al., 2016; Liu et al., 2012). The slope of the first calibration curve is denoted by *S*, and σ represents the standard deviation of the blank current. With σ = 0.00067 and S = 4.1901, the LOD was found to be 0.48 nM (*S*/*N* = 3, confidence level = 95%). As shown in Fig. 3B, it can be seen that the peak current of $CuCo_2O_4$/N-CNTs/NIP/GCE increases with higher MNZ concentration. Linear relationship is exhibited in the concentration range of 20–80 μM. The linear regression equation is I_p (μA) = 0.1864c (μM) - 3.0379, R^2 = 0.9989 (Fig. 3D, red curve). In comparison, the peak current of $CuCo_2O_4$/N-CNTs/NIP/GCE is lower than that of $CuCo_2O_4$/N-CNTs/MIP/GCE. This may be due to the higher binding capacity of MIP. Table 1 shows the comparison of this method with other methods for MNZ analysis. The analysis of MNZ by $CuCo_2O_4$/N-CNTs/MIP/GCE shows a wide linear range and low detection limits.

3.5.2. Selectivity

The chemical structure and size of the analyte are the two main factors affecting selectivity. Molecules with similar chemical structures and electrochemical properties may interfere with the specific recognition for MNZ. In addition, certain substances present in the sample may also have an impact. Under the optimal determination conditions, MNZ structural analogs such as p-nitrophenol, 1-methylimidazole, L-phenylalanine, glycine, carbamide, dimetridazole and 2-methyl-5-nitroimizazole present in biological samples were tested. 0.1 μM and 10 μM MNZ were evaluated separately, with the concentration of the interfering substances 100 times of MNZ concentration. As shown in Fig. 4, these substances have no significant impact on the determination of MNZ (peak current change value ≤ 5%). In addition, inorganic ions such as K^+, Na^+, Mg^{2+}, Ca^{2+}, Al^{3+}, Cl^-, SO_4^{2-} in 400 times concentration were tested, and found to have no significant interference with the detection of MNZ. The results indicate that the imprinted cavities in the MIP film specifically recognizes MNZ, and the prepared sensing system is highly selective toward MNZ. The specific binding constant K_{d1} and non-specific binding constant K_{d2} of $CuCo_2O_4$/N-

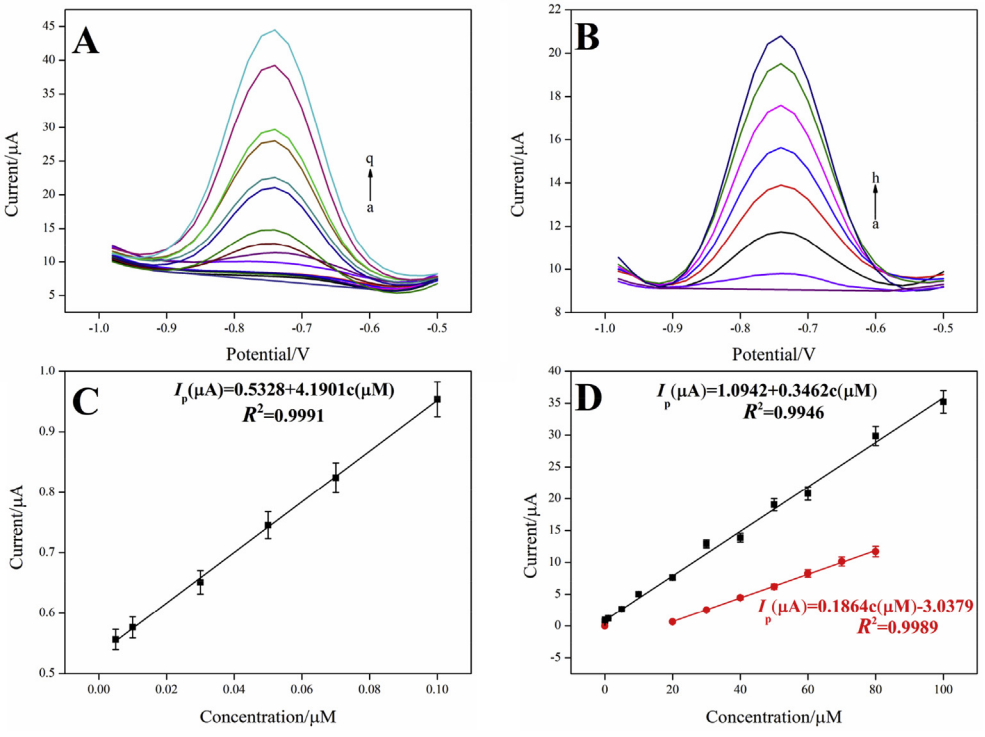

Fig. 3. (**A**) DPV characterization of a range of concentrations for MNZ (a–q): 0, 0.005, 0.01, 0.03, 0.05, 0.07, 0.1, 1, 5, 10, 20, 30, 40, 50, 60, 80, 100 μM on the $CuCo_2O_4$/N-CNTs/MIP/GCE in PBS (0.1 M, pH 10.0); (**B**) DPV characterization of a range of concentrations for MNZ (a–g): 0, 20, 30, 40, 50, 60, 70, 80 μM on the $CuCo_2O_4$/N-CNTs/NIP/GCE in PBS (0.1 M, pH 10.0); (**C**) and (**D**) Calibration curve between MNZ concentration and current response of sensors: the black curve represents $CuCo_2O_4$/N-CNTs/MIP/GCE, the red curve represents $CuCo_2O_4$/N-CNTs/NIP/GCE. (For interpretation of the references to colour in this figure legend, the reader is referred to the Web version of this article.)

Table 1
Comparison of this work with other methods for MNZ analysis.

Sensors	Methods	Linear range (μM)	Determination limit (μM)	Reference
optical nanosensor	[b]FES	0.2–15	0.15	(Mehrzad-Samarin et al., 2017)
MIP/AuNPs/GCE	DPV	0.5–1000	0.12	(Gu et al., 2016a)
HPLC	HPLC	[a]10–250	3.17[a]	(Gadallah et al., 2019)
MIP/2D Sn_3O_4 sensor	DPV	0.025–25	0.0032	(Wang et al., 2018a)
PrV/SCN/GCE	CV	0.001–2444	0.0008	(Kokulnathan and Chen, 2019)
Boron-doped diamond electrode	[c]SWV	0.2–42	0.065	(Ammar et al., 2016)
Fe_3O_4/N/C@MWCNTs	DPV	1–10 10–725	0.19	(Yuan et al., 2019)
GQDs-MIPs/GNPs/GCE	DPV	0.005–0.75 0.75–10.0	0.00052	(Ensafi et al., 2018b)
$CuCo_2O_4$/N-CNTs/MIP/GCE	DPV	0.005–0.1 0.1–100	0.00048	This work

[a] The unit of linear range and determination limit is ng·band^{-1}.
[b] FES stands for fluorescence emission spectra.
[c] SWV stands for square wave voltammetry.

CNTs/MIP/GCE for MNZ were 1.48 μmol L^{-1} and 4.91 μmol L^{-1}, respectively. The binding constant K_{d3} of $CuCo_2O_4$/N-CNTs/NIP/GCE for MNZ is 5.81 μmol L^{-1}. The binding constant K_{d4} of $CuCo_2O_4$/N-CNTs/MIP/GCE to dimetridazole was 5.62 μmol L^{-1}. The binding constant K_{d5} of $CuCo_2O_4$/N-CNTs/NIP/GCE to dimetridazole was 6.19 μmol L^{-1}. The calculation results are shown in Table S3. The values of K_{d2}, K_{d3}, K_{d4} and K_{d5} are close and are larger than K_{d1}, indicating that $CuCo_2O_4$/N-CNTs/MIP/GCE has high selectivity for MNZ (Gong et al., 2016; Wei et al., 2015; Zhou et al., 2013). This means that due to the presence of specific recognition sites for MNZ in MIP, MIP specifically adsorbs MNZ and non-specifically adsorbs to dimetridazole. NIP non-specifically adsorbs both MNZ and dimetridazole due to the lack of recognition sites. In addition, the calculation results of the selective coefficient (K) are shown in Table S2. The larger the selective coefficient, the higher the selectivity of the sensor (Zhou et al., 2013). Since MIP has molecularly imprinted cavities that specifically recognize MNZ, $CuCo_2O_4$/N-CNTs/MIP/GCE has a higher selectivity for MNZ. However, NIP lacks molecularly imprinted cavities that specifically recognize MNZ, so $CuCo_2O_4$/N-CNTs/NIP/GCE is less selective for MNZ. Supporting material details the binding constant and selective coefficient.

3.5.3. Reproducibility, repeatability and stability

In order to evaluate the reproducibility of electrochemical sensor, eight batches of $CuCo_2O_4$/N-CNTs/MIP/GCE were prepared in parallel. Under the optimal determination conditions, DPV determination was performed on 30 μM MNZ respectively, and the RSD was 3.2%, which indicates that the electrochemical sensor has good reproducibility. In addition, the same $CuCo_2O_4$/N-CNTs/MIP/GCE was repeatedly used for 30 μM MNZ by adsorption-elution-resorption process. The RSD value of current intensity was 4.7%, showing satisfactory repeatability. Similarly, in order to investigate the stability, DPV determination was performed on 30 μM MNZ. After two weeks of storage at room temperature, the peak current intensity is 96% of the initial current response, showing good stability. Excellent reproducibility, repeatability and stability make this electrochemical sensor promising for the quantitative analysis of MNZ.

3.5.4. Real sample analysis

The practicality of this sensor was evaluated by measuring different concentrations of MNZ in metronidazole tablets, human serum and urine. Supporting material details the preparation of real samples. The recovery test was carried out using standard addition methods. Each sample was measured three times under the same conditions. According to the Student T-test, the confidence level was 95%, the recovery rate of MNZ was 95.9%–100.9%, and the RSDs were in the range of 3.2%–4.8%. The accuracy of the assay was verified using HPLC methods (Rao et al., 2018b; Wang et al., 2018b). Table S1 lists the comparison results. The small differences between the two are within the error range, indicating that the the present electrochemical sensing system is reliable.

4. Conclusions

A novel molecularly imprinted electrochemical sensing system is developed for determination of MNZ with high sensitivity and selectivity. Two linear ranges were obtained in the concentration range of

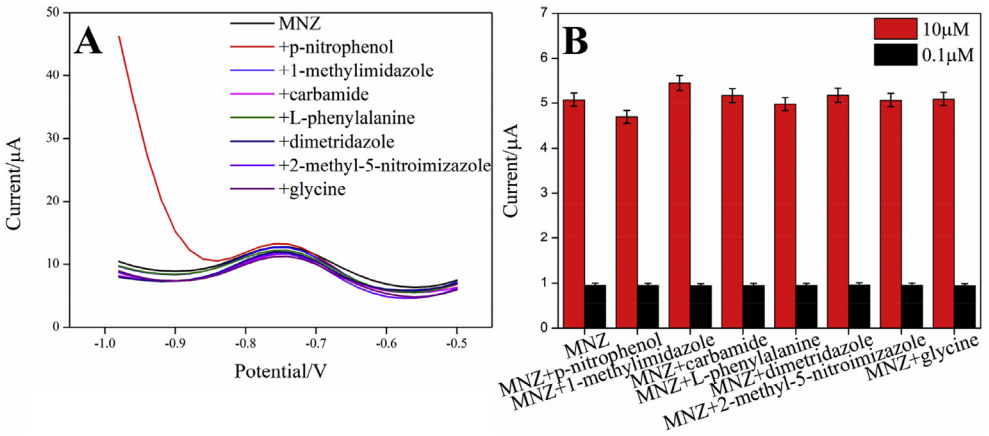

Fig. 4. (**A**) DPV of 10 μM MNZ and 100 μM p-nitrophenol, 1-methylimidazole, carbamide, L-phenylalanine, glycine, dimetridazole and 2-methyl-5-nitroimizazole; (**B**) DPV current responses of $CuCo_2O_4$/N-CNTs/MIP/GCE in MNZ and the analogues (n = 3).

0.005–0.1 μM and 0.1–100 μM with the LOD of 0.48 nM (S/N = 3). And calculate the binding constant K_d (1.48 μmol L^{-1}) and the selective coefficient K (4.48–98.47). In addition, the reliable recovery (95.9%–100.9%) and reasonable RSDs (3.2%–4.8%) in the analysis of real samples including metronidazole tablets, human serum and urine indicate the broad practicality of this sensing system. However, the limitation of the small number of molecularly imprinted cavities remain to be resolved. In the future, the use of multiple functional monomers can be explored to enhance the interaction between monomer and template molecules, and increase the quantities of effective cavities. The methodology reported herein has high potential for determination of MNZ in biomedical applications, and could be expanded to other target analytes.

Conflicts of interest statement

The authors declare that they have no conflicts of interest.

Declaration of interests

The authors declare that they have no known competing financial interests or personal relationships that could have appeared to influence the work reported in this paper.

CRediT authorship contribution statement

Yanying Wang: Conceptualization, Investigation, Formal analysis, Methodology, Writing - original draft. **Lang Yao:** Formal analysis, Writing - original draft. **Xin Liu:** Formal analysis. **Jing Cheng:** Formal analysis. **Wei Liu:** Formal analysis. **Tao Liu:** Writing - review & editing. **Mengmeng Sun:** Writing - review & editing. **Lijun Zhao:** Writing - review & editing. **Fang Ding:** Validation, Visualization. **Zhiwei Lu:** Writing - review & editing. **Ping Zou:** Validation, Visualization. **Xianxiang Wang:** Validation, Visualization. **Qingbiao Zhao:** Funding acquisition. **Hanbing Rao:** Conceptualization, Investigation, Formal analysis, Methodology, Data curation, Funding acquisition.

Acknowledgments

This work was funded by the Sichuan Agricultural University Research Interest Project (Project No. 2018324). Qingbiao Zhao was supported by National Natural Science Foundation of China (Grant No. 11404358).

Appendix A. Supplementary data

Supplementary data to this article can be found online at https://doi.org/10.1016/j.bios.2019.111483.

References

Alizadeh, T., Nayeri, S., Mirzaee, S., 2019. Talanta 192, 103–111.
Atar, N., Yola, M.L., Eren, T., 2016. Appl. Surf. Sci. 362, 315–322.
Ammar, H.B., Ben Brahim, M., Abdelhedi, R., Samet, Y., 2016. Mat. Sci. Eng. C-Mater. 59, 604–610.
Bari, V.R., Dhorda, U.J., Sundaresan, M., 1998. Anal. Chim. Acta. 376 (2), 221–225.
Beluomini, M.A., da Silva, J.L., Sedenho, G.C., Stradiotto, N.R., 2017. Talanta 165, 231–239.
Chen, D., Deng, J., Liang, J., Xie, J., Hu, C.H., Huang, K.H., 2013. Sensor. Actuator. B-Chem. 183, 594–600.
Ensafi, A.A., Nasr-Esfahani, P., Rezaei, B., 2018a. Sensor. Actuator. B-Chem. 270, 192–199.
Ensafi, A.A., Nasr-Esfahani, P., Rezaei, B., 2018b. Sensor. Actuator. B-Chem. 270, 192–199.
Gadallah, M.I., Ali, H.R.H., Askal, H.F., Saleh, G.A., 2019. Microchem. J. 146, 940–947.
Gao, Q., Wang, J.X., Wang, J.F., 2019. J. Alloy. Comp. 789, 193–200.
Gomes, F.O., Maia, L.B., Delerue-Matos, C., Moura, I., Moura, J.J.G., Morais, S., 2019. Sensor. Actuator. B-Chem. 285, 445–452.
Gong, C.B., Yang, Y.Z., Yang, Y.H., Zheng, A.X., Liu, S., Tang, Q., 2016. J. Colloid Interface Sci. 481, 236–244.
Gong, F.-C., Zhang, X.-B., Guo, C.-C., Shen, G.-L., Yu, R.-Q., 2003. Sensors 3 (4), 91–100.
Gu, Y., Yan, X., Li, C., Zheng, B., Li, Y., Liu, W., Zhang, Z., Yang, M., 2016a. Biosens. Bioelectron. 77, 393–399.
Gu, Y., Yan, X.Y., Li, C., Zheng, B., Li, Y.R., Liu, W.L., Zhang, Z.Q., Yang, M., 2016b. Biosens. Bioelectron. 77, 393–399.
Guo, W., Sun, W., Wang, Y., 2015. Acs. Nano. 9 (11), 11462–11471.
Hatamie, A., Marahel, F., Sharifat, A., 2018. Talanta 176, 518–525.
Jadhav, H.S., Pawar, S.M., Jadhav, A.H., Thorat, G.M., Seo, J.G., 2016. Sci. Rep-Uk. 6, 31120.
Joshi, A., Nagaiah, T.C., 2015. Rsc. Adv. 5 (127), 105119–105127.
Kim, H., Lee, K., Woo, S.I., Jung, Y., 2011. Phys. Chem. Chem. Phys. 13 (39), 17505–17510.
Kokulnathan, T., Chen, S.M., 2019. Acs. Appl. Mater. Inter. 11 (8), 7893–7905.
Li, Y., Liu, J., Liu, M., Yu, F., Zhang, L., Tang, H., Ye, B.-C., Lai, L., 2016. Electrochem. Commun. 64, 42–45.
Li, Y.C., Liu, Y., Yang, Y., Yu, F., Liu, J., Song, H., Liu, J., Tang, H., Ye, B.C., Sun, Z.P., 2015. Acs. Appl. Mater. Inter. 7 (28), 15474–15480.
Liu, J., Tang, H., Zhang, B., Deng, X., Zhao, F., Zuo, P., Ye, B.-C., Li, Y., 2016a. Anal. Bioanal. Chem. 408 (16), 4287–4295.
Liu, P., Zhang, X., Xu, W., Guo, C., Wang, S., 2012. Sensor. Actuator. B-Chem. 163 (1), 84–89.
Liu, S., San Hui, K., Hui, K.N., Yun, J.M., Kim, K.H., 2016b. J. Mater. Chem. A. 4 (21), 8061–8071.
Liu, S., San Hui, K., Hui, K.N., Yun, J.M., Kim, K.H., 2016c. J. Mater. Chem. A. 4 (21), 8061–8071.
Maldonado, S., Morin, S., Stevenson, K.J., 2006. Carbon 44 (8), 1429–1437.
Mehrzad-Samarin, M., Faridbod, F., Dezfuli, A.S., Ganjali, M.R., 2017. Biosens. Bioelectron. 92, 618–623.
Pandey, I., Kant, R., 2016. Biosens. Bioelectron. 77, 715–724.
Paraknowitsch, J.P., Thomas, A., 2013. Energy. Environ. Sci. 6 (10), 2839–2855.
Pawar, S.M., Pawar, B.S., Babar, P.T., Ahmed, A.T.A., Chavan, H.S., Jo, Y., Cho, S., Kim, J., Hou, B., Inamdar, A.I., Cha, S., Kim, J.H., Kim, T.G., Kim, H., Im, H., 2019. Appl. Surf. Sci. 470, 360–367.
Peng, J., Hou, C., Hu, X., 2012. Sensor. Actuator. B-Chem. 169, 81–87.
Rao, H., Zhao, X., Liu, X., Zhong, J., Zhang, Z., Zou, P., Jiang, Y., Wang, X., Wang, Y., 2018a. Biosens. Bioelectron. 100, 341–347.
Rao, H.B., Zhao, X., Liu, X., Zhong, J., Zhang, Z.Y., Zou, P., Jiang, Y.Y., Wang, X.X., Wang, Y.Y., 2018b. Biosens. Bioelectron. 100, 341–347.
Tong, Z., Yang, D., Shi, J., Nan, Y., Sun, Y., Jiang, Z., 2015. Acs. Appl. Mater. Inter. 7 (46), 25693–25701.
Wang, J., Du, W., Huang, X., Hu, J., Xia, W., Jin, D., Shu, Y., Xu, Q., Hu, X., 2018a. Anal. Method. Instrum. 10 (41), 4985–4994.
Wang, Y., Cheng, J., Liu, X., Ding, F., Zou, P., Wang, X., Zhao, Q., Rao, H., 2018b. Acs. Sustain. Chem. Eng. 6 (12), 16847–16858.
Wang, Y., Zhang, P., Jiang, N., Gong, X., Meng, L., Wang, D., Ou, N., Zhang, H., 2012. J. Chromatogr. B. 899, 27–30.
Wei, Y.B., Tang, Q., Gong, C.B., Lam, M.H.W., 2015. Anal. Chim. Acta. 900, 10–20.
Xiao, N., Deng, J., Cheng, J., Ju, S., Zhao, H., Xie, J., Qian, D., He, J., 2016. Biosens. Bioelectron. 81, 54–60.
Xu, K.B., Ma, S., Shen, Y.N., Ren, Q.L., Yang, J.M., Chen, X., Hu, J.Q., 2019. Chem. Eng. J. 369, 363–369.
Yuan, L., Jiang, L., Hui, T., Jie, L., Bingbin, X., Feng, Y., Yingchun, L., 2015. Sensor. Actuator. B-Chem. 206, 647–652.
Yuan, S., Bo, X.J., Guo, L.P., 2019. Talanta 193, 100–109.
Zhang, J., Sui, R., Xue, Y., Wang, X., Pei, J., Liang, X., Zhuang, Z., 2019. Sci. China. Mater. 62 (5), 690–698.
Zhang, J., Wang, Y., Lv, R., Xu, L., 2010. Electrochim. Acta. 55 (12), 4039–4044.
Zhang, Z., Cai, R., Long, F., Wang, J., 2015. Talanta 134, 435–442.
Zhou, H., Xu, Y.P., Tong, H.W., Liu, Y.X., Han, F., Yan, X.Y., Liu, S.M., 2013. J. Appl. Polym. Sci. 128 (6), 3846–3852.
Zhu, W., Yue, X., Duan, J., Zhang, Y., Zhang, W., Yu, S., Wang, Y., Zhang, D., Wang, J., 2016. Electrochim. Acta. 188, 85–90.